AGU ADVANCING EARTH AND SPACE SCIENCE

Water Resources Research

RESEARCH ARTICLE
10.1029/2020WR029450

Improvements to the Fracture Pipe Network Model for Complex 3D Discrete Fracture Networks

Chenhui Wang[1], Kejian Wu[1], and Gilbert Scott[2]

[1]School of Engineering, University of Aberdeen, Aberdeen, UK, [2]Anasuria Operating Company, Aberdeen, UK

Key Points:

- Fracture pipe network model (FPNM) is improved from four perspectives to improve the prediction accuracy
- Two indicators are proposed to quantify the complexity of discrete fracture networks (DFNs)
- The improved FPNM has been justified by synthetic DFNs and realistic fractured samples

Supporting Information:

Supporting Information may be found in the online version of this article.

Correspondence to:

C. Wang and K. Wu,
wangchenhui_upc@outlook.com;
kejian.wu@abdn.ac.uk

Citation:

Wang, C., Wu, K., & Scott, G. (2022). Improvements to the fracture pipe network model for complex 3D discrete fracture networks. *Water Resources Research*, *58*, e2020WR029450. https://doi.org/10.1029/2020WR029450

Received 14 DEC 2020
Accepted 16 FEB 2022

Author Contributions:

Conceptualization: Chenhui Wang, Kejian Wu, Gilbert Scott
Formal analysis: Chenhui Wang, Gilbert Scott
Methodology: Chenhui Wang, Kejian Wu, Gilbert Scott
Software: Chenhui Wang
Supervision: Kejian Wu
Validation: Chenhui Wang, Gilbert Scott
Visualization: Chenhui Wang
Writing – original draft: Chenhui Wang
Writing – review & editing: Chenhui Wang, Kejian Wu, Gilbert Scott

Abstract Fractures widely present in the subsurface and play a critical role in the fluid flow processes in porous media. The Fracture Pipe Network Model (FPNM) is an efficient method to represent and calculate fluid flow properties as a particular part of Discrete Fracture Networks (DFNs) method compared to direct numerical simulations. However, the current FPNM formulation can result in large deviations in computed fluid flow properties when applied to complex interconnected DFNs, although it can produce good results for simple DFNs. To enhance the performance and versatility of current FPNMs, four modifications to the FPNM formulation are introduced from different perspectives to improve the accuracy of pipe conductance assignment and ensure the correct topology of the fracture network. Two benchmarking examples with complex interconnected fractures and two real fractured samples are presented and the results show the modifications significantly improve the accuracy of computed fluid flow properties in complex DFNs.

1. Introduction

Fractures are widely existed in subsurface. They dominate the fluid flow in many types of media and have a huge impact on many subjects such as environmental engineering, groundwater engineering, geothermal energy and etc (Council, 2001; Rouchier et al., 2012; Watanabe et al., 1998). Hydraulic fracturing techniques are frequently used to improve the productivity of tight reservoirs to make the production of shale gas and oil possible (Medeiros et al., 2007; Roussel & Sharma, 2011). Hence, fractures dominate the geo-mechanical and hydrological behavior of many hydrocarbon reservoirs.

A well known and successful method to characterize fractures is the Discrete Fracture Network (DFN) model. This technique was proposed in the 1980s and developed afterward with various applications in civil, environmental and reservoir engineering (Berre et al., 2018; Long & Billaux, 1987; Robinson, 1984). DFN models are a reconstruction of the geometry of real fracture networks which preserve topology and use regular shapes to represent real fractures. The commonly used shapes include rectangular, disc, ellipse etc. The geometry of real fractures are simplified as fracture aperture, length and width (rectangular) or major and minor axes (ellipse). Generally, geometrical properties of fractures can be obtained on the basis of observations and measurements and from techniques such as X-ray micro-Computed Tomography or downhole tools like high resolution resistivity logging and borehole radar techniques (Serzu et al., 2004; Wu et al., 2020; Zhou et al., 2018). In addition, some researchers introduce roughness models into DFN, such as a joint roughness coefficient and fractal dimension models (Crandall et al., 2010; Jing et al., 2017; Lei et al., 2017). The topology of a fracture network is represented by the intersection points (in 2D) or intersection lines (or traces) (in 3D) of fractures, which are important for the network connectivity and fluid flow properties.

Various approaches have been developed to investigate the fractures' effect on fluid flow properties, for example, finite element method (FEM) (Elsworth, 1986; Köppel et al., 2019; Schädle et al., 2019), boundary element method (BEM) (Dershowitz & Fidelibus, 1999), finite volume method (FVM) (Berre et al., 2021; Flemisch et al., 2018), fracture pipe network model (FPNM) (Cacas et al., 1990; Dershowitz & Fidelibus, 1999), etc. The finite element method imposes a mesh over the individual fractures before solving the fluid field from Stoke's equation within fractures. Finite element method need mesh all of the fracture volume and apply denser mesh close to the intersection lines between fractures, which would be computationally expensive. The evolving non-conforming mesh technique overcomes the problems of conforming mesh. Independent discretizations for the fractures and matrix can be generated to achieve high flexibility and avoid the tedious fine-tuning of the conforming mesh (Schädle et al., 2019). While boundary element method overcomes this problem, as it only discretizes the fracture external boundary and the intersection lines with other fractures. The fracture pipe network model

represents fractures as pipes with equivalent hydraulic conductivity. These three methods can also be combined to achieve better functionality. For example, Elsworth (1986) proposed a hybrid boundary element-finite element method to analyze fluid flow in DFNs. Dershowitz and Fidelibus (1999) used the boundary element method to calculate the equivalent conductance of fracture pipe element and then adopetd the fracture pipe network model to calculate the flow properties.

In this research, FPNM is selected for the following three reasons. First, the pipe model is straightforward because each fracture is represented by a hydraulically equivalent pipe element. Second, FPNM is easy to implement as it does not need a complex mesh process. Third, FPNM is computationally efficient compared to lattice-Boltzmann simulations in the predictions of fluid flow properties.

In general, direct numerical simulations (DNS) can be used to compare with fracture pipe network models. DNS methods include the direct simulations of fluid flow or computational fluid dynamics to solve the Navier–Stokes equation. They include the traditional grid-based methods, for example, finite difference method and finite element method (Flemisch et al., 2018), as well as particle-based methods, for example, lattice Boltzmann method (Latt et al., 2020).

A key issue of FPNM construction is the estimation of the hydraulically equivalent pipe element parameters. We reviewed the literature and found most researchers used a common method to generate fracture pipe networks. We call this the centroid and intersection line method (CIM) (e.g., Guo et al., 2018; Jing et al., 2020; Ren et al., 2016; Tsang & Tsang, 1987, and others). However, the common formulation of CIM/FPNM results in large deviations in computed fluid flow properties when applied to complex interconnected DFNs. This will be discussed in later sections. This paper contains a number of proposals to circumvent this problem and improve the accuracy and versatility of current fracture pipe network models.

The structure of this paper is below. In Section 2, we firstly introduce the general procedures to construct a FPNM. Then, the procedures to calculate permeability by the FPNM are provided. A numerical method is introduced to compare with the FPNM. In Section 3, the commonly used FPNM model is discussed through a simple DFN and a complex DFN test case. Two parameters are introduced to quantify the complexity of the DFN structure. Then, the four general modifications to the current FPNM formulation are elaborated to improve the FPNM model when applied to complex DFNs. In Section 4 presents two benchmarking DFN scenarios and two realistic fractured samples to compare and justify the improved FPNM with a lattice Boltzmann method. And then, the improved fracture pipe network model is discussed in terms of its application scope and limitations. In Section 5 summarizes our conclusions.

2. Methodology

In this section, the general procedures to build a fracture pipe network from a DFN is first introduced. Then, the fluid flow model is presented that is, the flow equations, initial conditions, boundary conditions and solution method. Finally, we demonstrate the four improvements to our new fracture pipe network model.

2.1. Construction of Fracture Pipe Network

The centroid and intersection line method (CIM) of constructing a FPNM is described as follows. Figure 1 shows an illustration of a simple fracture pipe network, where fractures are represented as ellipses. The intersection between fracture planes is called an intersection line or trace. A pipe element is built between the centroid point of each fracture and the midpoint of the intersection line, as shown in Figure 1. Each pipe is further divided into two node elements connected by one bond element, for example, in fracture F2. The reason for this is that the intersection between fractures locally enlarges the flow path, while the flow in the middle part of fractures is not affected. The research of Sarkar et al. (2004) shows that fluid flow aligns with the fracture orientation, regardless of the direction of the global pressure gradient. This effect can only be applied on the boundary of fractures, namely, the node elements. This will be discussed further below.

From the fluid flow point, each pipe represents a seepage subdomain of fluid flow. As shown in Figure 1, the subdomain represents the part of fracture from its centroid to the intersection line. The next step is to convert each subdomain into an equivalent rectangular domain so that an analytical fluid flow solution can be applied directly. The most common approach is to use the well known “cubic law” which is the analytical solution of Stoke's

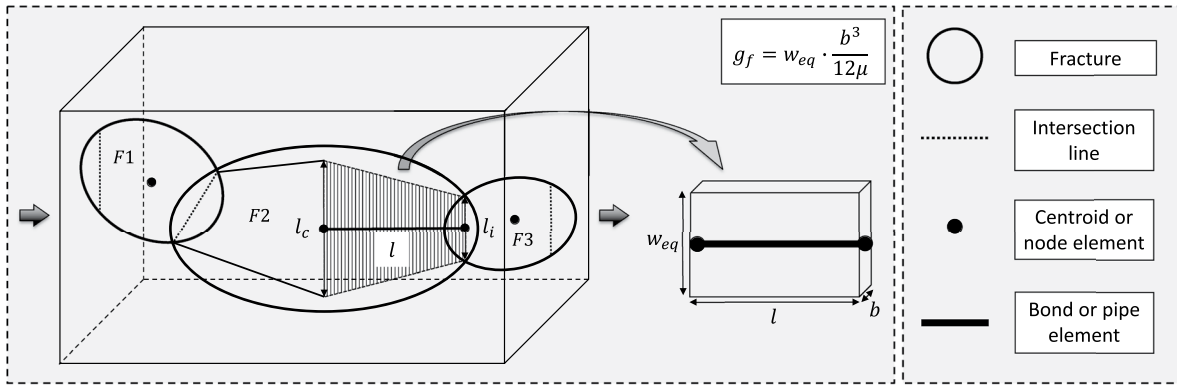

Figure 1. Illustration of a simple Discrete Fracture Networks with three ellipse shape fractures, the centroid points, intersection lines, fracture pipe elements, and seepage subdomain (the shaded zone) which is transformed into equivalent rectangular seepage subdomain and then represented by the fracture pipe elements. g_f is the hydraulic conductance of the equivalent rectangular fracture. b, w_{eq}, l are the fracture aperture, equivalent width and length.

Equation 1 and the mass balance Equation 2 for incompressible laminar flow between infinite parallel planes with a no-slip boundary condition (Witherspoon et al., 1980):

$$\mu\nabla^2\vec{u} - \nabla P = 0 \tag{1}$$

$$\rho\nabla u = 0 \tag{2}$$

where μ is the dynamic viscosity, $\vec{u}$ is the fluid velocity, P is the pressure and ρ is the fluid density.

In this research, we focus on the pore scale laminar flow. The Reynolds number is defined as:

$$\mathrm{Re} = \frac{\rho\vec{u}b}{\mu} \tag{3}$$

where b is the fracture aperture. It is the characteristic pore length in rock fracture system as used by many researchers. The Reynolds number values reported in the literature for the nonlinear flow in rough fractures are less than 20 (Quinn et al., 2020).

Guo et al. (2018) derived the equations for the equivalent rectangular element for disc like fracture, which will be referred as Guo's model in the later sections. They first proposed an equation to calculate the length of the centroid node:

$$l_c = \frac{2D}{N_i} \cdot \frac{l_i}{\overline{l_i}} \tag{4}$$

where D is the diameter of the disc shaped fracture, N_i is number of intersection lines on the fracture, l_i is the intersection line length and $\overline{l_i}$ is the average length of all intersection lines on the fracture.

The equivalent rectangular fracture parameters can be obtained by applying Darcy's law for each seepage subdomain, where two seepage domains produce the same flow rate under the same boundary conditions. The equivalent width of the rectangle is:

$$w_{eq} = \frac{l_c - l_i}{\ln(l_c/l_i)} \tag{5}$$

Hence, the conductance for each fracture pipe is obtained from the cubic law:

$$g_f = w_{eq} \cdot \frac{b^3}{12\mu} \tag{6}$$

where b is the fracture aperture.

By applying the above equations, the parameters of each pipe element can be calculated and the fracture pipe network is consequently constructed.

2.2. Calculation of Fluid Flow Properties

Fluid flow can be simulated directly in the fracture pipe network. This section introduces the assumptions used in the fluid flow simulation. Single phase incompressible laminar flow is considered and an analytical solution of the Stoke's equation is incorporated via the pipe conductances as discussed above.

A constant pressure boundary condition is applied to the model inlet and outlet, and the other faces of the model are assumed no-flow boundaries. Fluid pressures are defined at the center of the node elements and pressure drop occurs across bonds between the connected nodes. The flow rate Q_{ij} between two nodes is given by:

$$Q_{ij} = \frac{g_{ij}}{L_{ij}} (P_i - P_j) \tag{7}$$

where g_{ij} is the harmonic mean conductance between two node elements i, j and a bond element k given by:

$$g_{ij} = \frac{L_{ij}}{\frac{L_i}{g_i} + \frac{L_j}{g_j} + \frac{L_k}{g_k}} \tag{8}$$

Mass conservation is imposed for each node element i:

$$\sum_{j}^{N_i} Q_{ij} = 0 \tag{9}$$

where j runs over all the bond elements connecting to the node element i. Combining Equations 7 and 9, a linear set of equations can be defined and solved for the node pressures. The number of equations and the number of unknowns is equal to the number of node elements. The linear equations are solved using the algebraic solver in OpenCV (Bradski, 2000).

With the pressure known at the center of each node element, the total flow rate Q_t is found by calculating the average flow rate along the inlet and outlet, and the absolute permeability k of the network is found from Darcy's law:

$$k = \frac{Q_t \mu L}{A \Delta P} \tag{10}$$

2.3. Reference Numerical Method

Lattice Boltzmann Method (LBM) is used to benchmark the fracture pipe network model. LBM simulations were performed in Palabos, an open-source computational fluid dynamics (CFD) solver based on the C++ (Latt et al., 2020). The permeability was determined from LBM simulations of steady state single-phase flow.

It can be shown that the LBM is equivalent to the solution of the N–S equation assuming that density variations and the Mach number are small (Chen & Doolen, 1998). Hence the theoretical framework of LBM means it can predict accurate simulation results for single phase laminar flow. However, LBM is a numerical method, indicating that simulation results by LBM also have numerical errors. Pan et al. (2006) did systematic quantitative comparisons of the numerical accuracy and convergence rate of the LBM when modeling fluid flow in sphere packs. Results show that permeabilities simulated by LBM are dependent on the image spatial resolution and the choice of the relaxation parameters. The smaller the pore size or the coarser the grid is, the larger the errors are. But for most cases of pore scale fluid flow simulations, LBM can still serve as a reasonable reference numerical method to benchmark other methods.

The following parameters were used for the LBM simulations in this study. The D3Q19 discrete velocity scheme and the multiple-relaxation-time models (MRT) were used. The initial conditions are zero fluid velocity and a constant pressure gradient in the principal flow direction. Bounce-back boundary conditions are applied at the solid walls and constant pressures are applied at the inlet and outlet. The pressure difference is set as 0.0001 in

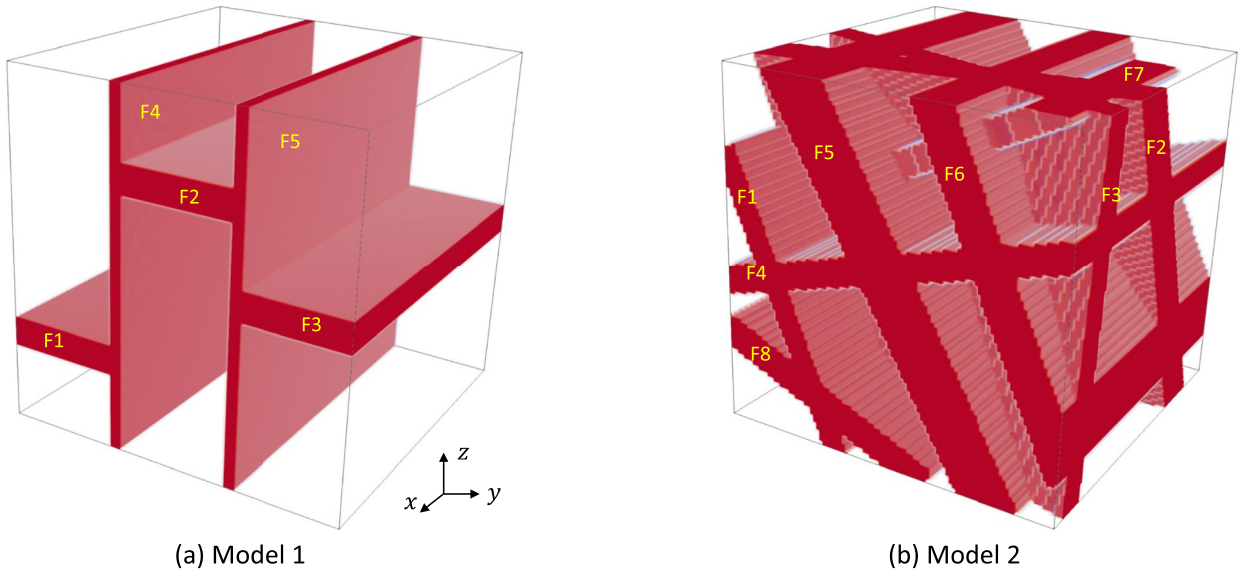

Figure 2. The two Discrete Fracture Networks test cases used to validate Guo's model. Model 1 has 5 regular fracture and model 2 has 8 oriented fractures. The model size is 100^3 voxels, and image resolution is 1 μm/voxel.

lattice unit. The typical value of collision operator omega 1.0 is used and kinematic viscosity is 0.16667. In all cases the simulation converged to a steady state in less than 10,000 iterations.

3. The Improved FPNM

This section introduces the improved fracture pipe network model. We firstly analyze the problems of the commonly used FPNM through a simple DFN and a complex DFN test case. Then, we introduce the four specific improvements made on the current FPNM formulation to improve its performance when applied to complex DFNs.

3.1. Benchmarking of the Traditional FPNM

To investigate Guo's model, two different DFNs are constructed, as shown in Figure 2. The model size is 100^3 voxels and the image resolution is 1 μm/voxel. The permeabilities are calculated both from the FPNM and directly from the 3D voxel volume using a lattice Boltzmann Method (LBM) (Latt et al., 2020).

Guo's model assumes fracture are disc shape, while these two models use rectangular fractures. Therefore, the diameter used in Equation 4 for the centroid node length, becomes:

$$D = \sqrt{\frac{4A}{\pi}} \tag{11}$$

where A is the area of the rectangular fracture, that is, the product of fracture width and length.

The permeabilities calculated from FPNM using Guo's equations and the LBM simulations are shown in Table 1. The percentage deviation is calculated from:

$$\text{deviation} = \frac{k_{\text{FPNM}} - k_{\text{LBM}}}{k_{\text{LBM}}} \times 100\% \tag{12}$$

It is clear that Guo's model predicts accurate permeabilities for model 1 but has large deviations for model 2. The difference between these two network lies in the complexity of fracture intersections. To quantify the complexity of DFN structures, we propose two complexity indicators.

The first indicator is the average intersection line number:

Table 1
Permeabilities Calculated From Fracture Pipe Network Model and LBM Respectively for the Two Discrete Fracture Networks Test Cases

	k_x (mD)		k_y (mD)		k_z (mD)	
Model name	FPNM	LBM	FPNM	LBM	FPNM	LBM
Model 1	862.73	893.27	128.73	135.68	223.93	223.88
Deviation (%)	−3.42	–	−5.12	–	0.02	–
Model 2	4952.05	8378.33	3322.0	6543.52	5215.94	9309.14
Deviation (%)	−40.89	–	−49.23	–	−43.97	–

$$\overline{N_{il}} = \frac{\sum N_{il}}{2N_f} \tag{13}$$

The second indicator is the average intersection point number:

$$\overline{N_{ip}} = \frac{\sum N_{ip}}{2N_f} \tag{14}$$

where *il* stands for the intersection lines and *ip* is the intersection points for a fracture, N_f is the total number of fractures. Note that counting the intersection lines number includes the six bounding surfaces, and divided by 2 is because each intersection is shared by two fractures.

The average intersection line number for these two model are 3.8 and 6.0 respectively, and the average intersection point number for the two models are 0 and 6.13. In general, the larger these two parameters are, the more complex the DFN is. It shows that DFN test Case 2 has more complex structure than model 1. And Guo's model has large deviations for a complex DFN. To improve the performance and versatility of the FPNM, we propose four modifications from different perspectives.

3.2. Improvements Made on the New FPNM

Before introducing the improvements to the FPNM, the examples of DFN scenarios studied in this section should be introduced. The second example of DFN scenario in the previous section is separated into six sub-models in order of increasing complexity of DFN structures. Figure 3 displays the six sub models and Table 2 shows their complexity indicators.

Guo's model is applied on these six DFN scenarios to compute the permeabilities and the results are shown in Table 3. The average deviation is calculated for the *X*, *Y* and *Z* directions and plotted in Figure 4 for all models. Results show that Guo's model has large discrepancies with LBM and the deviations increase with increased complexity indicator of DFNs.

3.2.1. First Improvement: Centroid Node Length

From Figure 4, we can see that the permeability from Guo's model is smaller than the LBM permeability. The main reason is that the conductance assigned to the fracture pipe elements is too small, which is furthermore related to the equivalent width and centroid node length.

For simple DFN, the number of fracture intersections is small and does not have a large effect on the length calculation. But for complex DFN, the number of intersection lines N_i increases dramatically, which decreases centroid node length and equivalent width, and thus the permeabilities are decreased significantly. The fact that permeability deviations for the six sub DFN scenarios increase with increased complexity indicators also reflects this trend. Therefore, the first improvement we made to Guo's fracture pipe network model is a modification of the centroid node length. The N_i is removed from the denominator shown in Equation 4 for the reason above, and the modified formula of centroid node length is:

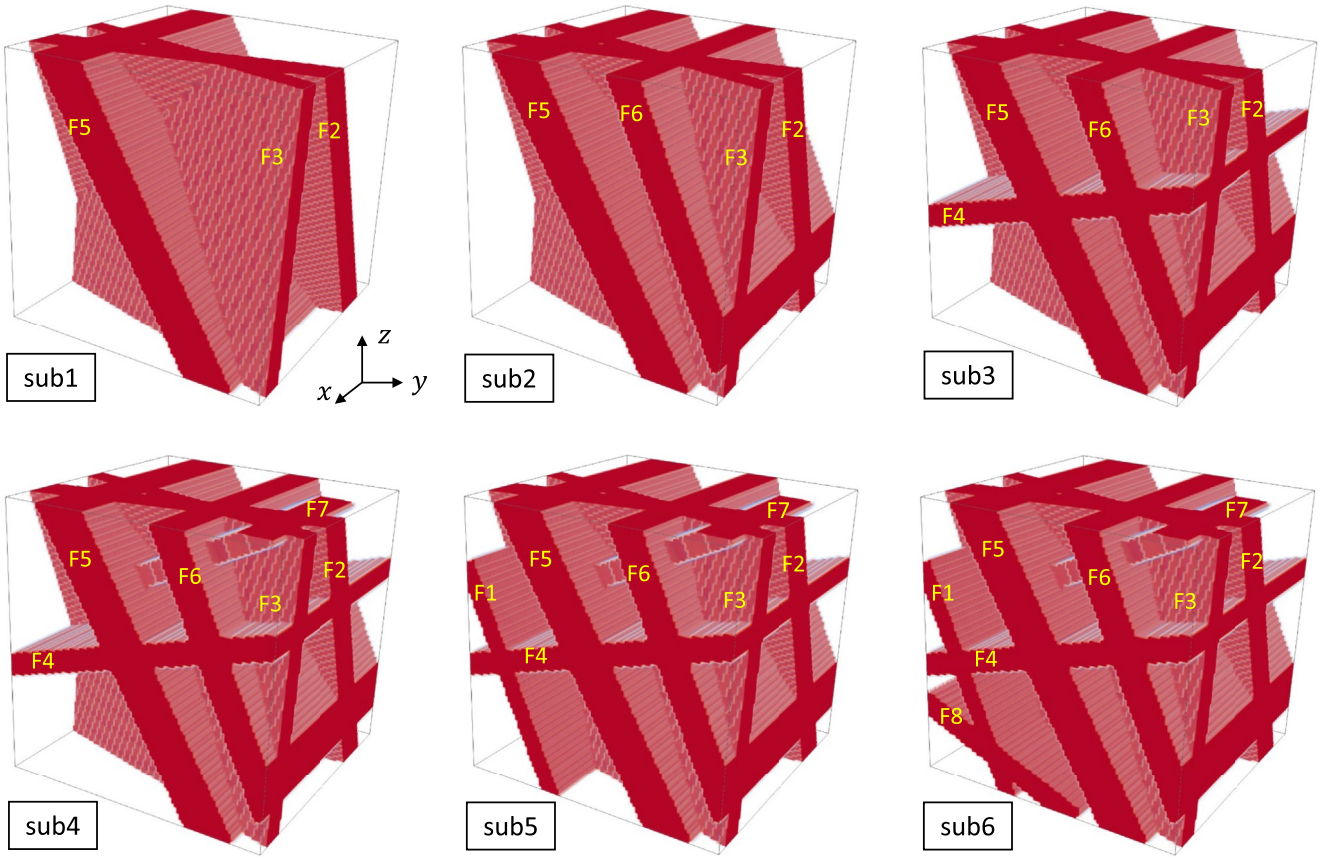

Figure 3. Illustration of the six sub Discrete Fracture Networks scenarios.

$$l_c = \sqrt{\frac{4A}{\pi}} \cdot \frac{l_i}{\overline{l_i}} \tag{15}$$

The first improvement is applied on the FPNM and the average deviation with LBM results are calculated and shown in Figure 4. The simulated permeabilities of the network and deviations data can be found in Table S1. It is clear that the results are improved. The average deviation for all six models is calculated, which is reduced from −35% to −18%, with around 17% improvement.

In addition, Figure 5 shows a comparison between the equivalent width and diameter for fractures in DFN scenario sub6. We can see the equivalent width of fractures calculated by our model is larger than Guo's model. DFN scenario sub6 only has 8 fractures, but its average intersection line number is 6.0 as shown in Table 2. This will significantly reduce the centroid node length calculated for the DFN scenario sub6 as well the equivalent width, therefore, the calculated permeability will be lower than the LBM. From Figure 5, we can conclude that the equivalent rectangular seepage subdomain should have consistent equivalent width and consistent fracture diameter so that the flow pattern of the original seepage subdomain can be represented.

Table 2
Complexity Indicators for the Six Sub Discrete Fracture Networks Scenarios

	sub1	sub2	sub3	sub4	sub5	sub6
$\overline{N_{il}}$	5.0	5.25	5.8	5.67	5.86	6.0
$\overline{N_{ip}}$	1.0	0.75	3.0	5.0	6.0	6.13

3.2.2. Second Improvement: Boundary Node Length

As shown in Figure 6, the boundary nodes constructed for the pipe network are half spheres while the inner nodes are whole spheres, and pressure is defined on the node center. These two kind of nodes are handled using the same strategy, that is, boundary nodes are treated as whole spheres, so there is extra pressure loss on boundary nodes. This issue can be solved easily by

Table 3
Permeabilities Calculated From Fracture Pipe Network Model and LBM Respectively for the Six Sub Discrete Fracture Networks Scenarios

	k_x (mD)		k_y (mD)		k_z (mD)	
Model name	FPNM	LBM	FPNM	LBM	FPNM	LBM
sub1	3933.88	4854.66	3542.11	4459.88	6413.53	7244.41
Deviation (%)	−18.97	–	−20.58	–	−11.47	–
sub2	5237.03	6152.01	3416.78	4911.36	6348.34	8176.29
Deviation (%)	−14.87	–	−30.43	–	−22.36	–
sub3	4729.33	7122.32	3355.46	5741.8	5384.77	8443.32
Deviation (%)	−33.60	–	−41.56	–	−36.22	–
sub4	4290.75	7343.8	3106.05	5956.25	4957.27	8632.74
Deviation (%)	−41.57	–	−47.85	–	−42.58	–
sub5	4542.01	7743.75	3120.47	6192.96	5007.89	9020.16
Deviation (%)	−41.35	–	−49.61	–	−44.48	–
sub6	4952.05	8378.33	3322.0	6543.52	5215.94	9309.14
Deviation (%)	−40.89	–	−49.23	–	−43.97	–

still keep the boundary nodes as whole spheres, while reducing the connected bond length by the boundary node radius, that is, $l_{b_{new}} = l_{b_{old}} - r_n$, where the l_b is the bond length and r_n is the boundary node radius.

By applying the second improvement, the average deviation with LBM results are calculated and shown in Figure 4. The average deviation for all six models is reduced from −18% to −7%, with around 11% improvement.

3.2.3. Third Improvement: Node Cross-Sectional Area

When two fractures intersect, their intersection area will be greater than the original cross-sectional area within either fracture. This is another reason why pipe network permeabilities are lower than LBM results. We propose the dihedral angle θ between two intersecting fractures to calculate the node area, which is defined as the the angle between the normal vector of the two fractures and can be calculated from:

$$\theta = \arccos\left(\frac{|\overrightarrow{n_{f1}} \cdot \overrightarrow{n_{f2}}|}{|\overrightarrow{n_{f1}}| \cdot |\overrightarrow{n_{f2}}|}\right) \tag{16}$$

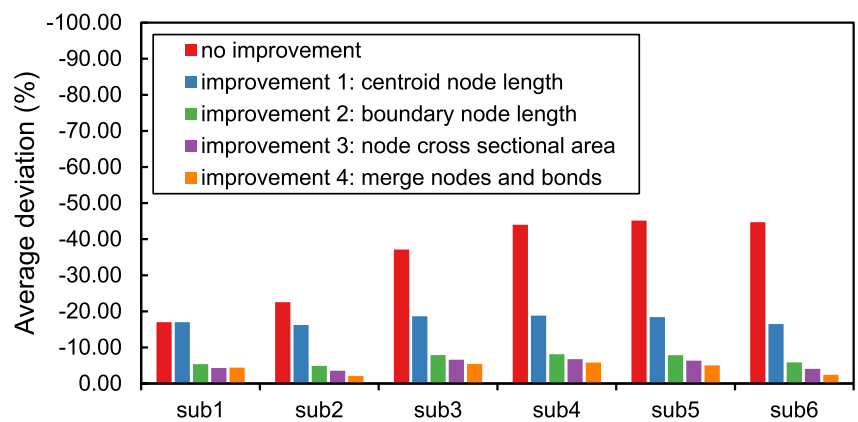

Figure 4. Average deviation of permeabilities for the six sub Discrete Fracture Networks scenarios calculated by Fracture Pipe Network Model and compared to LBM results.

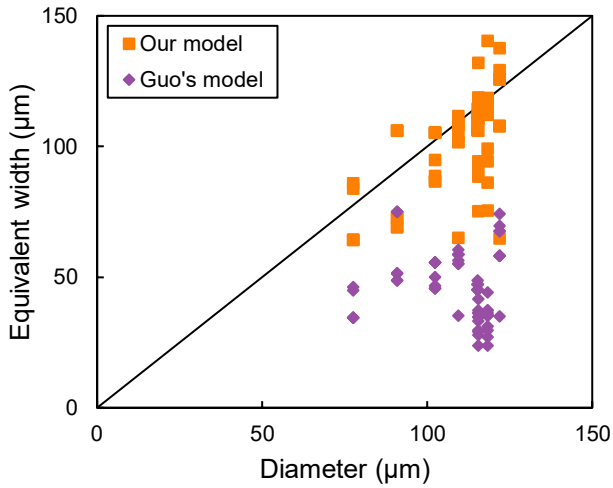

Figure 5. Comparison between equivalent width and diameter for Discrete Fracture Networks scenario sub6, where equivalent width is calculated from our model and Guo's model separately, and diameter is calculated from Equation 11.

In Guo's model the cross-sectional area of a node is simply calculated as: $A = b_1 \cdot b_2$, but in our model the cross-sectional area is $A = (b_1 \cdot b_2)/\sin(\theta)$. Because conductance is generally scaled with square area $g \sim A^2$, the updated conductance is:

$$g \sim \frac{1}{(\sin(\theta))^2} \tag{17}$$

After applying this third improvement on all sub DFN scenarios, the average deviation with LBM results were calculated and shown in Figure 4. The average deviation for all six models is reduced from −7% to −5.6%, with around 1.4% improvement.

This improvement is slight, because the enlarged intersection area is only applied to node elements and not bond elements. The study of Sarkar et al. (2004) shows that fluid flow aligns with the fracture orientation, regardless of the direction of the pressure gradient. Therefore, the cross-sectional area of the middle part of the fracture (where the bond element is constructed from) should not be modified.

3.2.4. Fourth Improvement: Merge Nodes and Bonds

The fourth improvement is pertaining to the network construction process itself. Because of the complexity of fracture intersections, some nodes and bonds overlap or even locate at the same position, which affects the pipe network structure and fluid flow simulations. Therefore, we apply post processing to the pipe network to selectively merge nodes and bonds to make sure the network topology is correct. This step is automated in our own software codes using C++.

As shown in Figure 7, there are some special cases when node or bond elements should be merged. The first case (Figure 7a) is when two fracture centroid points overlap and the two centroid nodes locate close, that is, the distance between two centroids is less than half of the fracture aperture, which would create a problem of bond construction and the network topology would be incorrect. The solution for this case is to only leave one node which would not affect the fluid flow simulation but can ensure the correct topology of the fracture pipe network.

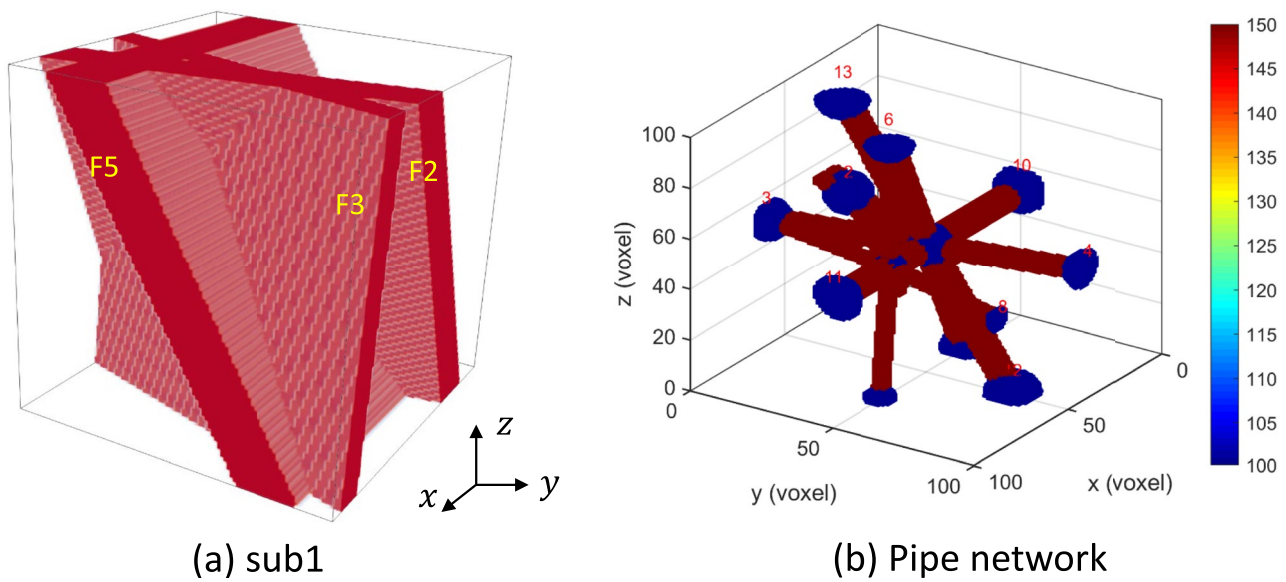

Figure 6. (a) The Discrete Fracture Networks scenario sub1 and (b) its corresponding pipe network, where blue spheres represent nodes and red cylinders are bonds, the number above spheres are the nodes index.

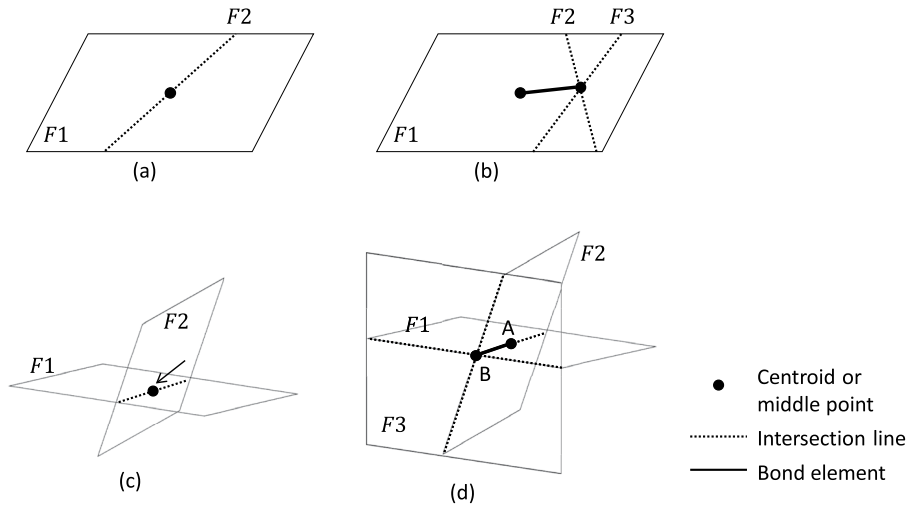

Figure 7. Illustration of the special cases when nodes and bonds should be merged.

The second case (Figure 7b) is when the middle points of two intersection lines overlap. Bonds constructed from fracture F1 to fracture F2 and F3 will cause repetition, so one bond needs to be deleted.

For the third case (Figure 7c), fracture 1 centroid is overlapped with the middle point of the intersection line. According to the pipe network construction process, there would be a bond between each centroid and intersection line. Therefore, this case will create a bond connected from a node to itself, so this redundancy needs to be deleted.

The fourth case (Figure 7d) is quite special. Fracture 1 and 2 centroid points overlap and their intersection lines with fracture 3 also overlap. When constructing a bond from fracture 1 and 2 to fracture 3 (between point A to B), the bonds are repeated, but they cannot be deleted because they are from different fractures. These two bonds should be merged using the superposition principle on the conductance, that is, add their conductance and assign to the bond.

The node and bond post processing was applied to all DFN scenarios and the average permeability deviation with LBM results were calculated and shown in Figure 4. The average deviation for all six models is reduced from −5.6% to −4.5%, with around 1.1% improvement. Although this improvement is slight, the post processing procedure is essential to achive the correct topology of the pipe network.

4. Results and Discussions: Benchmarking With Idealized and Realistic Scenarios

In this section, we justify the improved FPNM model by two benchmarking scenarios with complex connected fractures, which are stochastically constructed by an open source code. Then, the improved FPNM is applied on two realistic fractured carbonate samples. Finally, the improved FPNM is discussed in terms of the pros and cons.

4.1. Benchmarking Cases

Alghalandis (2017); Alghalandis (2018) developed an open source code (ADFNE) to generate and analyze discrete fracture networks. The code (version 1.5) was used to generate synthetic DFNs to validate our modifications to the fracture pipe network model. Two benchmarking DFN examples were constructed as shown in Figure 8.

The testing case S1 has 74 fractures and case S2 has 157 fractures. A square fracture shape is used and the fracture side length follows an exponential distribution. The length ranges from 0.2 to 0.8 unit length (which is later scaled to 20 to 80 microns) with the mean value of the exponential distribution as 0.3. All fracture apertures are set as 5 microns for case S1 and 7 microns for S2. Connectivity analysis was then applied to remove isolated fractures and to make sure the DFN is fully percolating for the purposes of fluid flow simulation. The DFNs shown in Figure 8

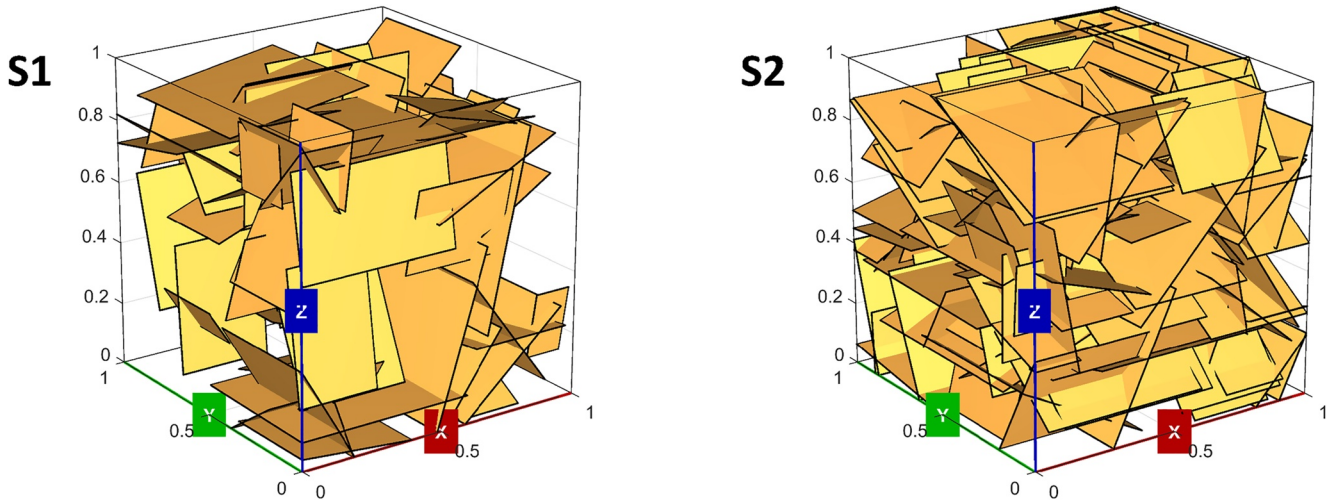

Figure 8. Two benchmarking Discrete Fracture Networks examples generated by ADFNE open source code.

are fully percolating in all 3 directions. In addition, the average intersection line number for these two model are 3.81 and 5.79 respectively, and the average intersection point number for the two models are 3.62 and 15.75. It is clear both of them are complex interconnected DFNs.

To start, the angle of fracture orientation distribution for the two DFNs are analyzed and the results are plotted in Figure 9. The angle is defined between the fracture normal vector and the *X*, *Y*, *Z* axes. If the angle is 90°, it means the fracture is parallel to the axis. If the angle is 0°, then the fracture is perpendicular to the axis. Analysis of the angle frequency distributions for the two benchmarking models show that the angles peak in 80° to 100° with X and *Y* axes, while the angles are close to uniformly distributed for *Z* axis for both models. This means that fractures are generally aligned closer to the *X* and *Y* axes.

Then, FPNMs are extracted from these two DFNs and the four improvements above were applied. Figure 10 (b) shows the extracted fracture pipe network. The permeabilities are calculated from both the pipe network model and LBM. For comparison, Guo's pipe network model was applied to compute the permeabilities from the same DNFs. Results are reported in Table 4. The permeabilities calculated by the improved fracture pipe network model show excellent agreement with LBM while Guo's model has large discrepancies.

In addition, on a personal laptop (Intel Core i7 CPU, 32 GB RAM), the computation time for the fracture pipe network model (a couple of seconds) is much faster than that of the corresponding LBM solution (average is 500 s). It can be seen that the four improvements proposed in this study significantly improve the performance of fracture pipe network models, and particularly for complex connected discrete fracture networks.

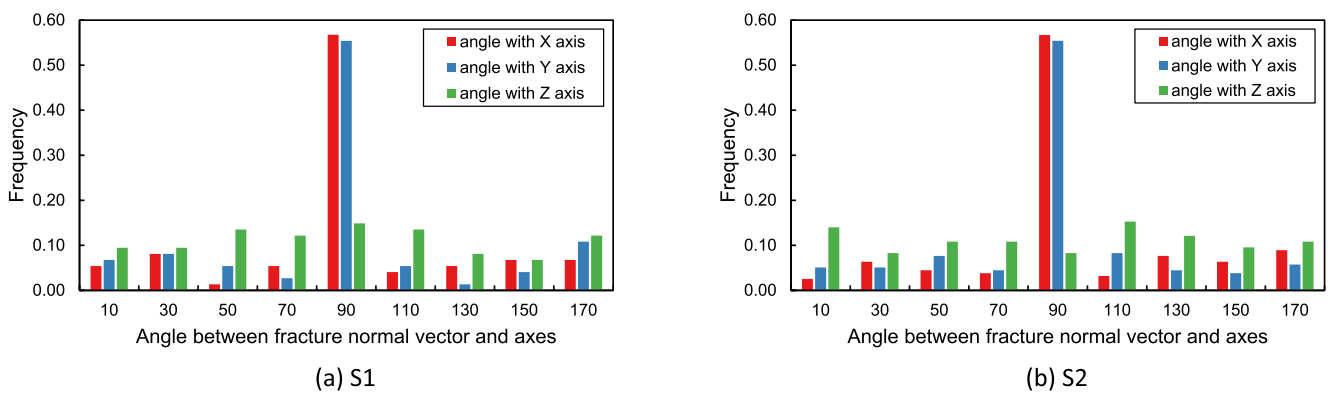

Figure 9. The angle frequency distribution for the two benchmarking Discrete Fracture Networks examples, which is defined between the fracture normal vector and the *X*, *Y*, *Z* axes.

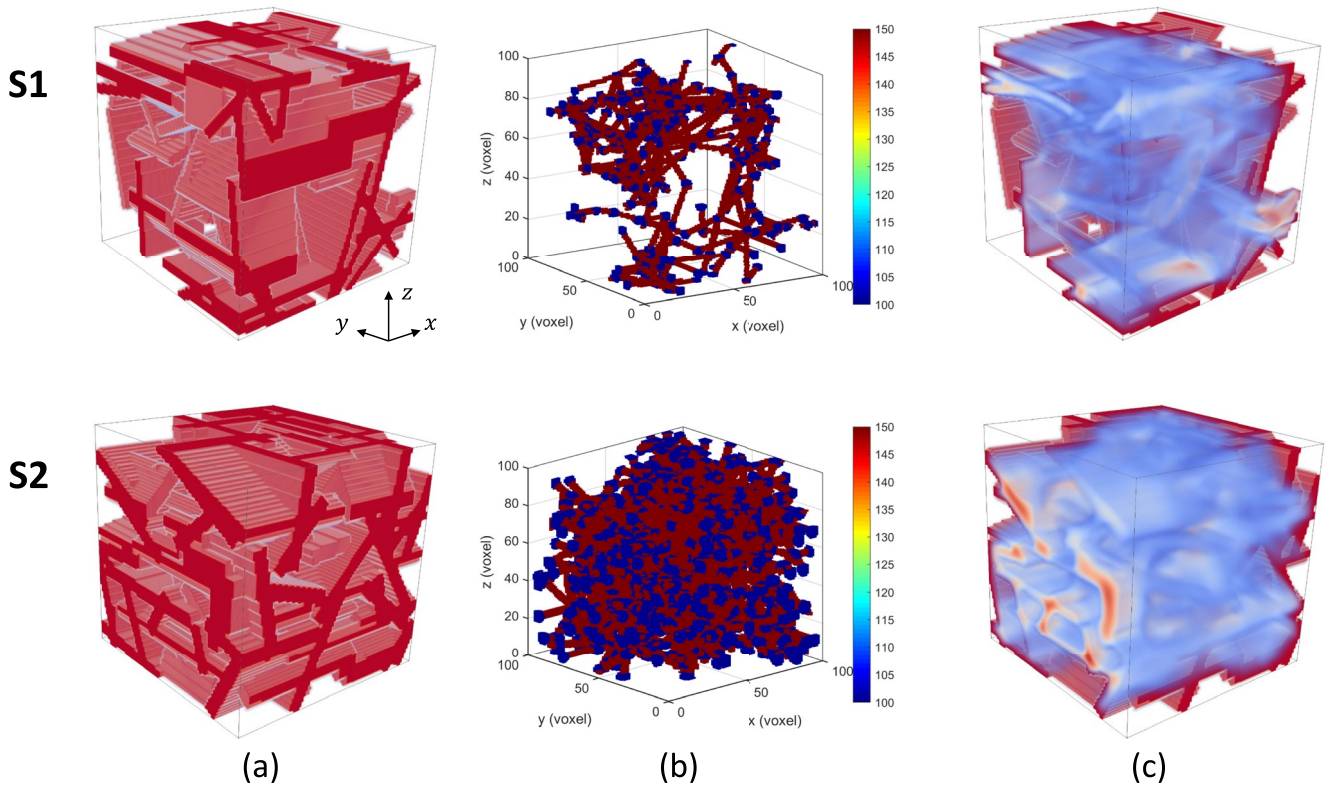

Figure 10. (a) Two benchmarking Discrete Fracture Networks cases, S1 has 74 fractures and S2 has 157 fractures. The size of both models is 100^3 voxels and the image resolution is 1 μm/voxel. (b) The corresponding fracture pipe networks, where blue spheres are nodes and red cylinders are bonds. (c) The velocity profile along *X* direction simulated by LBM.

4.2. Real-World Case Study

Two fractured samples are used to demonstrate the applicability of the improved FPNM model. The micro-CT images of these samples are from a carbonate rock reservoir. The reservoir formation rock is tight and the original matrix porosity is enhanced by micro-fractrues and small scale faults networks. The representative discrete fracture networks are extracted with idealized fracture geometric and topological properties by hand using the ImageJ (Fiji) (Schindelin et al., 2012). Figure 11 shows the micro-CT images and the equivalent DFNs, where the case R1 has two intersecting fractures and case R2 has four fractures. For the permeability calculation, the small isolated fractures are removed from the fracture network.

Table 4
Permeabilities (unit: millidarcy (mD)) for the Two Benchmarking Discrete Fracture Networks Examples Calculated From Fracture Pipe Network Model and LBM Respectively

Model name	Method name	k_x (mD)	k_y (mD)	k_z (mD)
Model 1	DFN (LBM)	238.98	184.27	182.197
	FPNM (ours)	216.74	168.22	161.71
	Deviation with DFN (%)	−9.31	−8.71	−11.24
	FPNM (Guo's)	95.19	75.27	64.17
	Deviation with DFN (%)	−60.17	−59.15	−64.78
Model 2	DFN (LBM)	4842.34	5951.23	3455.11
	FPNM (ours)	4598.78	5594.29	3165.57
	Deviation with DFN (%)	−5.03	−7.51	−8.38
	FPNM (Guo's)	1651.81	2049.86	1139.63
	Deviation with DFN (%)	−65.89	−65.56	−67.02

Similarly, the Guo's model and the improved FPNM model are applied on the two DFN test cases. Table 5 shows the permeability results that are calculated from the DFNs and FPNMs. We can see that for most of the cases, the improved FPNM can predict more accurate permeability results than the Guo's model when compared to the results of LBM.

However, permeability deviations in real-world cases are larger than the benchmarking cases. The deviations involved usually come from several aspects. On the one hand, they are from the assumptions made in the model. In the current work, cubic law is adopted as the analytical solution to model the fluid flow in fractures. This may result in deviations when simulating the fluid flow in a real-world fracture system. On the other hand, the deviations may come from the simulation of LBM. The accuracy of LBM simulation depends on the number of lattices used in the model. The fewer the simulation lattices it has, the larger errors it would result in. For example, real-world

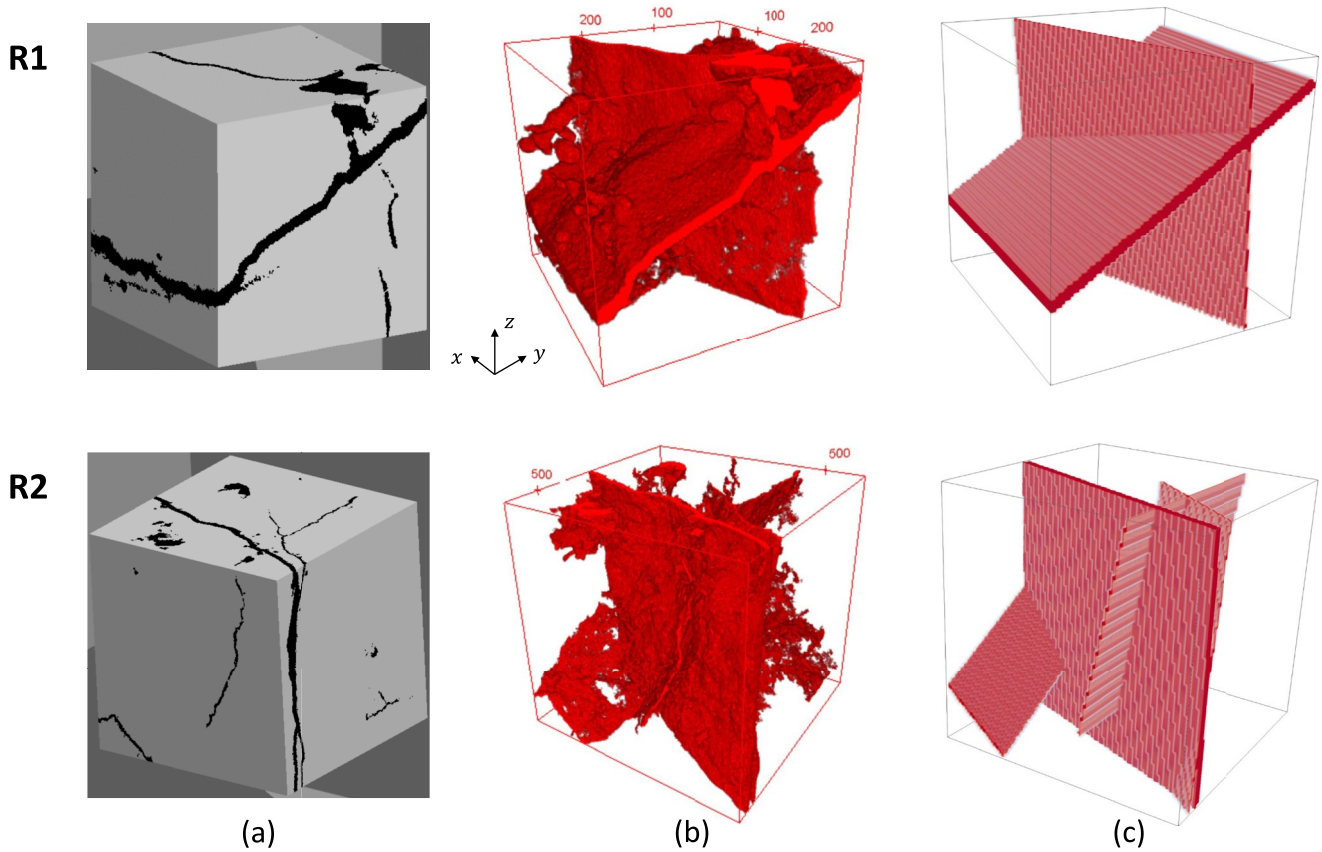

Figure 11. The micro-CT images of the realistic fractured samples R1 and R2 (a and b) and the corresponding equivalent Discrete Fracture Networks (c). The image size for R1 and R2 is 300^3 and 600^3 voxels respectively. Image resolution is 13 μm/voxel for both samples.

Table 5
Permeabilities (unit: darcy (D)) for the Two Fractured Samples That Are Calculated From the Discrete Fracture Networks (DFN) and the Fracture Pipe Network Model (FPNM), Where the DFN Results Are Simulated by the LBM and FPNM Results Are Computed by the Model Proposed in This Paper

Model name	Method name	k_x (D)	k_y (D)	k_z (D)
Case R1	DFN (LBM)	71.32	49.20	2.00
	FPNM (ours)	80.78	59.19	1.69
	Deviation with DFN (%)	13.27	20.31	−15.50
	FPNM (Guo's)	86.04	62.70	2.42
	Deviation with DFN (%)	20.64	27.45	21.00
Case R2	DFN (LBM)	39.46	0.00	55.68
	FPNM (ours)	44.78	0.00	45.61
	Deviation with DFN (%)	13.48	–	−18.08
	FPNM (Guo's)	54.32	0.00	59.22
	Deviation with DFN (%)	37.66	–	6.36

Note. It should be noted that the fractures are not percolated in the *Y* direction for the case R2, and that's why $k_y = 0$.

case R2 has four fractures, while the minimum aperture size is only 4 voxels compared to the model size of 600 voxels. In this case, LBM could result in simulation errors.

4.3. Discussions on the Model

The essence of the fracture pipe network model is to divide fractures into flow subdomains and transform them into equivalent pipes. The flow in ideal DFNs, where fractures have regular shape and constant aperture, is identical for each subdomain. Therefore, the flow in the fracture can be well represented by pipe elements. In the improved FPNM, we consider the single-phase steady-state laminar flow rather than the turbulent flow, so that linear flow equations between the flow rate and pressure difference can be obtained.

The identification and extraction of fractures directly from micro-CT images and transformation to DFNs are challenging. This paper focuses on the fluid flow in DFNs principally. The improvements made on the new FPNM model are concentrating on the conductance assignment and the topology of the fracture networks, which are important to the fluid flow.

The DFN test cases used in this paper are ideal and regular fractures which do not include the fracture aperture variations and the roughness. Also, the

model only considers fully opened fractures, however, natural fractures are not always fully open as the precipitation of minerals inside fractures could seal and close fractures.

Currently, the model can only be applied to fractures without the pore matrix. The inclusion of the pore matrix in the FPNM is an important topic and we have developed a new model to consider both discrete fractures and pore matrix. This work will be presented in an upcoming paper.

5. Conclusions

In this research, we have shown that fracture pipe network models can be used to represent and calculate fluid flow properties of fracture networks. The fracture pipe network model constructed by Guo's method produces good results only for simple connected DFNs but results in large permeability errors when applied to complex DFNs.

Two simple indicators are proposed to quantify the complexity of DFN structures. In general, the larger the DFN complexity indicator, the more complex the DFN structure is.

Four modifications are proposed to improve the performance and versatility of fracture pipe network models. Two benchmarking examples are presented and the results show the new FPNM modifications significantly improve the accuracy of computed permeability in complex DFNs.

In addition, a real-world case study is performed. Two fractured carbonate samples are utilized to demonstrate that the improved FPNM model can be of use for the real-world applications.

Fracture pipe network models are straightforward to be built, and they require substantially less computational cost to simulate fluid flow compared with direct numerical simulations such as LBM. It is concluded that fracture pipe network modeling has significant potential to expand the scope and utility of practical DFN applications.

In further research, we plan to extend this work to investigate fracture/matrix flow by coupling FPNM with pore network modeling (Scott et al., 2019; Wang et al., 2020). The inclusion of the fracture roughness model will also be considered.

Data Availability Statement

For the data availability, the data that support the findings of this research are available in Mendeley data repository (Wang, 2020). All of the parameters of the DFNs (the coordinates, the aperture of the DFNs) used are available in http://dx.doi.org/10.17632/c8r645tj9v.2.

Acknowledgments
Chenhui Wang thanks the financial support from China Scholarship Council (CSC) for his Ph.D. study. The authors thank the discussions of the real-world case study with Dr Yu Jing at the University of New South Wales.

References

Alghalandis, Y. F. (2017). Adfne: Open source software for discrete fracture network engineering, two and three dimensional applications. *Computers & Geosciences*, *102*, 1–11. https://doi.org/10.1016/j.cageo.2017.02.002

Alghalandis, Y. F. (2018). *DFNE practices with ADFNE (Tech. Rep.)*. Alghalandis computing. Retrieved from http://alghalandis.net

Berre, I., Boon, W. M., Flemisch, B., Fumagalli, A., Gläser, D., Keilegavlen, E., et al. (2021). Verification benchmarks for single-phase flow in three-dimensional fractured porous media. *Advances in Water Resources*, *147*, 103759. https://doi.org/10.1016/j.advwatres.2020.103759

Berre, I., Doster, F., & Keilegavlen, E. (2018). Flow in fractured porous media: A review of conceptual models and discretization approaches. *Transport in Porous Media*, *130*(1), 215–236. https://doi.org/10.1007/s11242-018-1171-6

Bradski, G. (2000). The OpenCV library. *Dr. Dobb's journal of software tools*. Retrieved from https://opencv.org/

Cacas, M. C., Ledoux, E., de Marsily, G., Tillie, B., Barbreau, A., Durand, E., et al. (1990). Modeling fracture flow with a stochastic discrete fracture network: Calibration and validation: 1. The flow model. *Water Resources Research*, *26*(3), 479–489. https://doi.org/10.1029/WR026i003p00479

Chen, S., & Doolen, G. D. (1998). Lattice Boltzmann method. *Annual Review of Fluid Mechanics, 30* (Kadanoff 1986), 329–364. https://doi.org/10.1146/annurev.fluid.30.1.329

Council, N. (2001). *Conceptual models of flow and transport in the fractured vadose zone*. National Academies Press.

Crandall, D., Bromhal, G., & Karpyn, Z. T. (2010). Numerical simulations examining the relationship between wall-roughness and fluid flow in rock fractures. *International Journal of Rock Mechanics and Mining Sciences*, *47*(5), 784–796. https://doi.org/10.1016/J.IJRMMS.2010.03.015

Dershowitz, W. S., & Fidelibus, C. (1999). Derivation of equivalent pipe network analogues for three-dimensional discrete fracture networks by the boundary element method. *Water Resources Research*, *35*(9), 2685–2691. https://doi.org/10.1029/1999WR900118

Elsworth, D. (1986). A hybrid boundary element-finite element analysis procedure for fluid flow simulation in fractured rock masses. *International Journal for Numerical and Analytical Methods in Geomechanics*, *10*(6), 569–584. https://doi.org/10.1002/nag.1610100603

Flemisch, B., Berre, I., Boon, W., Fumagalli, A., Schwenck, N., Scotti, A., et al. (2018). Benchmarks for single-phase flow in fractured porous media. *Advances in Water Resources*, *111*, 239–258. https://doi.org/10.1016/j.advwatres.2017.10.036

Guo, L., Hu, X., Wu, L., Li, X., & Ma, H. (2018). Simulation of fluid flow in fractured rocks based on the discrete fracture network model optimized by measured information. *International Journal of Geomechanics*, *18*(10), 05018008. https://doi.org/10.1061/(ASCE)GM.1943-5622.0001270

Jing, Y., Armstrong, R. T., & Mostaghimi, P. (2017). Rough-walled discrete fracture network modelling for coal characterisation. *Fuel*, *191*, 442–453. https://doi.org/10.1016/j.fuel.2016.11.094

Jing, Y., Armstrong, R. T., & Mostaghimi, P. (2020). Image-based fracture pipe network modelling for prediction of coal permeability. *Fuel*, *270*, 117447. https://doi.org/10.1016/j.fuel.2020.117447

Köppel, M., Martin, V., Jaffré, J., & Roberts, J. E. (2019). A Lagrange multiplier method for a discrete fracture model for flow in porous media. *Computational Geosciences*, *23*(2), 239–253. https://doi.org/10.1007/s10596-018-9779-8

Latt, J., Malaspinas, O., Kontaxakis, D., Parmigiani, A., Lagrava, D., Brogi, F., et al. (2020). Palabos: Parallel lattice Boltzmann solver. *Computers and Mathematics with Applications*. https://doi.org/10.1016/j.camwa.2020.03.022

Lei, Q., Latham, J. P., & Tsang, C. F. (2017). The use of discrete fracture networks for modelling coupled geomechanical and hydrological behaviour of fractured rocks. *Computers and Geotechnics*, *85*, 151–176. https://doi.org/10.1016/j.compgeo.2016.12.024

Long, J. C. S., & Billaux, D. M. (1987). From field data to fracture network modeling: An example incorporating spatial structure. *Water Resources Research*, *23*(7), 1201–1216. https://doi.org/10.1029/WR023i007p01201

Medeiros, F., Ozkan, E., & Kazemi, H. (2007). Productivity and drainage area of fractured horizontal wells in tight gas reservoirs. In *Rocky mountain oil & gas technology symposium*. Society of Petroleum Engineers. https://doi.org/10.2118/108110-MS

Pan, C., Luo, L. S., & Miller, C. T. (2006). An evaluation of lattice Boltzmann schemes for porous medium flow simulation. *Computers & Fluids*, *35*(8–9), 898–909. https://doi.org/10.1016/j.compfluid.2005.03.008

Quinn, P. M., Cherry, J. A., & Parker, B. L. (2020). Relationship between the critical Reynolds number and aperture for flow through single fractures: Evidence from published laboratory studies. *Journal of Hydrology*, *581*, 124384. https://doi.org/10.1016/J.JHYDROL.2019.124384

Ren, F., Ma, G., Wang, Y., & Fan, L. (2016). Pipe network model for unconfined seepage analysis in fractured rock masses. *International Journal of Rock Mechanics and Mining Sciences*, *88*, 183–196. https://doi.org/10.1016/j.ijrmms.2016.07.023

Robinson, P. C. (1984). *Connectivity, flow and transport in netawork models of fractured media (Unpublished doctoral dissertation)*. University of Oxford.

Rouchier, S., Janssen, H., Rode, C., Woloszyn, M., Foray, G., & Roux, J. J. (2012). Characterization of fracture patterns and hygric properties for moisture flow modelling in cracked concrete. *Construction and Building Materials*, *34*, 54–62. https://doi.org/10.1016/j.conbuildmat.2012.02.047

Roussel, N. P., & Sharma, M. M. (2011). Optimizing fracture spacing and sequencing in horizontal-well fracturing. *SPE Production & Operations*, *26*(2), 173–184. https://doi.org/10.2118/127986-PA

Sarkar, S., Toksöz, M. N., & Burns, D. R. (2004). *Fluid flow modeling in fractures (Tech. Rep.)*. Massachusetts Institute of Technology. Retrieved from http://hdl.handle.net/1721.1/68616

Schädle, P., Zulian, P., Vogler, D., Bhopalam, S. R., Nestola, M. G., Ebigbo, A., et al. (2019). 3D non-conforming mesh model for flow in fractured porous media using Lagrange multipliers. *Computers & Geosciences*, *132*, 42–55. https://doi.org/10.1016/j.cageo.2019.06.014

Schindelin, J., Arganda-Carreras, I., Frise, E., Kaynig, V., Longair, M., Pietzsch, T., et al. (2012). Fiji: An open-source platform for biological-image analysis. *Nature Methods*, *9*(7), 676–682. https://doi.org/10.1038/nmeth.2019

Scott, G., Wu, K., & Zhou, Y. (2019). Multi-scale image-based pore space characterisation and pore network generation: Case study of a north sea sandstone reservoir. *Transport in Porous Media*, 1–30. https://doi.org/10.1007/s11242-019-01309-8

Serzu, M. H., Kozak, E. T., Lodha, G. S., Everitt, R. A., & Woodcock, D. R. (2004). Use of borehole radar techniques to characterize fractured granitic bedrock at AECL's Underground Research Laboratory. *Journal of Applied Geophysics*, *55*(1–2), 137–150. https://doi.org/10.1016/j.jappgeo.2003.06.012

Tsang, Y. W., & Tsang, C. F. (1987). Channel model of flow through fractured media. *Water Resources Research*, *23*(3), 467–479. https://doi.org/10.1029/WR023i003p00467

Wang, C. (2020). Data for "Improvements to the fracture pipe network model for complex 3D discrete fracture networks" (Mendeley Data; Version V2) [Data set]. https://doi.org/10.17632/c8r645tj9v.2

Wang, C., Wu, K., Scott, G. G., Akisanya, A. R., Gan, Q., & Zhou, Y. (2020). A new method for pore structure quantification and pore network extraction from SEM images. *Energy and Fuels*, *34*(1), 82–94. https://doi.org/10.1021/acs.energyfuels.9b02522

Watanabe, U., Imamura, Y., & Iida, I. (1998). Liquid penetration of precompressed wood VI: Anatomical characterization of pit fractures. *Journal of Wood Science*, *44*(2), 158–162. https://doi.org/10.1007/BF00526263

Witherspoon, P. A., Wang, J. S., Iwai, K., & Gale, J. E. (1980). Validity of Cubic Law for fluid flow in a deformable rock fracture. *Water Resources Research*, *16*(6), 1016–1024. https://doi.org/10.1029/WR016i006p01016

Wu, P., Li, Y., Sun, X., Liu, W., & Song, Y. (2020). Pore-scale 3D morphological modeling and physical characterization of hydrate-bearing sediment based on computed Tomography. *Journal of Geophysical Research: Solid Earth*, *125*(12). https://doi.org/10.1029/2020jb020570

Zhou, H. W., Zhong, J. C., Ren, W. G., Wang, X. Y., & Yi, H. Y. (2018). Characterization of pore-fracture networks and their evolution at various measurement scales in coal samples using X-ray μCT and a fractal method. *International Journal of Coal Geology*, *189*, 35–49. https://doi.org/10.1016/j.coal.2018.02.007